MRS Energy & Sustainability

doi:10.1557/s43581-026-00154-9

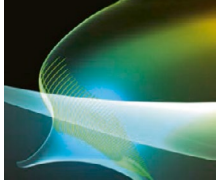

MATERIALS CHALLENGES AND ML-DRIVEN INNOVATION IN NEXT GENERATION CLEAN ENERGY—ORIGINAL RESEARCH

Thermoelectric effect in MoS_2/$MoSe_2$ heterostructures: Experimental evidence and theoretical aspects

Oscar A. López-Galán, **Francisco Sáenz Soto**, **Jorge L. Trimmer-Duarte**, **Luis C. Rubio-Dalli** and **Manuel Ramos**, Departamento de Física y Matemáticas, Instituto de Ingeniería y Tecnología, Universidad Autónoma de Ciudad Juárez, Avenida del Charro 450 N, Ciudad Juárez, Chihuahua 32310, México

John Nogan, Center for Integrated Nanotechnologies, Sandia National Laboratories, 1101 Eubank Bldg. SE, Albuquerque, NM 87110, USA

Alejandra Ramírez, Department Interface Design, Helmholtz-Zentrum Berlin Für Materialien Und Energie, GmbH, Hahn-Meitner-Platz 1, 14109 Berlin, Germany; Energy Materials In-Situ Laboratory Berlin (EMIL), Helmholtz-Zentrum Berlin Für Materialien Und Energie GmbH, Hahn-Meitner-Platz 1, 14109 Berlin, Germany

Roberto Félix Department Interface Design, Helmholtz-Zentrum Berlin Für Materialien Und Energie, GmbH, Hahn-Meitner-Platz 1, 14109 Berlin, Germany

José Mireles García Jr., Departamento de Ingeniería Eléctrica y Computación, Instituto de Ingeniería y Tecnología, Universidad Autónoma de Ciudad Juárez, Avenida del Charro 450 N, Ciudad Juárez, Chihuahua 32310, México

Roberto Carlos Ambrosio Lazaro, Facultad de Ciencias de La Electrónica, Benemerita Universidad Autónoma de Puebla, Ciudad Universitaria, Puebla 72570, México

Martin Heilmaier, Institute for Applied Materials and Materials Science, Karlsruhe Institute of Technology (KIT), Engelbert-Arnold-Str. 4, 76131 Karlsruhe, Germany

Mauricio Terrones, Department of Physics and Center for 2-Dimensional and Layered Materials, The Pennsylvania State University, University Park, PA 16802, USA

Abel Hurtado-Macías and **Roberto P. Talamantes-Soto**, Laboratorio Nacional de Nanotecnología, Centro de Investigación en Materiales Avanzados S.C., Miguel de Cervantes 120, Complejo Industrial Chihuahua, C.P. 31109 Ciudad Chihuahua, Chihuahua, Mexico

Address all correspondence to Oscar A. López-Galán at oscar.lopez@uacj.mx
Manuel Ramos at manuel.ramos@uacj.mx

(Received: 20 October 2025; accepted: 10 February 2026)

ABSTRACT

Transition metal dichalcogenides offer a rich platform to exploit overlooked thermoelectric potential for energy-recovery systems and hybrid energy harvesting. This work highlights the potential of MoS_2/$MoSe_2$ thin films for thermoelectric applications, featuring a low-cost, scalable, and excellent heterostructure formation that will guide future research in the field of energy and sustainability.

Efficient energy harvesting for applications such as radioisotope thermoelectric generators and heat-recovery systems require novel thermoelectric materials with exceptional performance. This work demonstrates thermoelectric capabilities of *n*-type MoS_2/$MoSe_2$ heterojunctions fabricated by scalable radiofrequency sputtering. These heterostructures demonstrated an outstanding experimental Seebeck coefficient of ~ – 1.1 mV K^{-1} (ΔT = 40 K), arising from thermally activated carriers with a low activation energy of 32 meV, and estimated thermoelectric figure-of-merit (*ZT*) values of ~ 1.0. Furthermore, computational calculations within framework of Density Functional Theory corroborate experimental findings allowing to elucidate a crucial role of atomic-scale in determining anisotropic thermoelectric properties. Lastly, our data indicate MoS_2/$MoSe_2$ heterojunctions are a promising material for low-cost and efficient thermoelectric for microelectronic devices.

Keywords heterostructure · thin film · thermoelectric · energy and sustainability

Introduction

The transition metal dichalcogenides (TMDCs) caused much attention mainly in thin films form, due to its viability offer toward development of applications such as sensors,[1] and detectors[2]; among the most common two-dimensional materials is molybdenum disulfide (MoS_2), demonstrating a remarkable level of integrality in solid-state and heterojunction technology[3] and solar energy harvesting.[4] Progress made in fabrication techniques, mainly for radiofrequency (RF)-sputtering processes for thin-film heterojunctions in large-scale applications by our group and others.[5–7] Reports indicate the potential use of MoS_2 in thermoelectric applications by enhancing thermoelectric response of TMDC multilayer structures, attributed to interface formation,[8–10] which is of relevance for development of technologic applications, including thermoelectric generators,[11] heating units (RHUs),[12] and heat-recovery systems.[10] For practical applications of TMDC as thermoelectric materials, it is necessary to determine their thermoelectric properties and their dependency on geometric arrangements and heterojunction formation, as this remains a vague aspect of current research. As Goldsmith indicates, to develop reliable thermoelectric generators, one needs a material with a thermal conductivity < 1.0 W m^{-1} K^{-1} to improve the thermoelectric performance through the dimensionless figure-of-merit *ZT* value and a reliable Seebeck coefficient value.[13] One preferred route to attain such a reduced thermal conductivity (κ) is to achieve a solid solution or to enhance phonon scattering due to interface formation. In principle, the different atomic weights of the constituent elements of the solid solution will facilitate phonon scattering. Similarly, current state-of-the-art research focuses on interfaces within the material, such as engineering grain boundaries, heterojunctions, or nanostructured semiconductors, which induce phonon scattering, thereby stopping heat propagation and reducing thermal energy transmission along the material.[14] Lan et al. fabricated sputtered amorphous MoS_2 films that exhibit thermal conductivities around 0.5 W m^{-1} K^{-1} and determined a minimal influence of the film thickness on the thermal conductivity.[15] This remarkably low thermal conductivity can be attributed to an increase in phonon dispersion resulting from the amorphous lattice. Ashraf et al. determine values of κ for the MoS_2 film of approximately 0.26 W m^{-1} K^{-1}, based on Fourier's law of conduction,[16] and these values are in agreement with previous reports by Muratore et al., indicating that (002)- and (100)-oriented MoS_2 films exhibit anisotropic κ values of 0.25–1.5 W m^{-1} K^{-1}, respectively. These results can be related to the scattering at domain boundaries that dominate

Discussion

- An ongoing effort using material science techniques to deliver viable, large-area, low-cost thin films with capacity for usage as thermoelectric generators with Seebeck coefficient ~ – 1.1 mV K-1 (ΔT = 40 K), as experimental measured by Van der Pauw method.
- Transition metal dichalcogenide thin films achieving high-quality, consistent heterostructure formation when deposited using conventional RF-sputtering from commercial targets at 99.9%.
- Among approaches to control thermoelectricity generation includes interface formation, yet few experimental–theoretical studies focus on transition metal dichalcogenides (TMDC) thin films for thermoelectricity generation are found in the literature.

phonon conduction in nanostructured TMD films; the Seebeck coefficient (S) in monolayer MoS_2 has been measured to be in the order of 1×10^2 μV K^{-1} with applied gate voltage (± 20 V), and this S is considerably larger than those measured for bulk MoS_2.[17] The predicted values of S by computational calculations for MoS_2 reach values of 1×10^3 μV K^{-1} when sulfur vacancies are present according to Sharma et al.,[18] and to the same order of magnitude in Van der Waals and Janus TMDC heterojunctions as extensively reported by others.[19,20] These studies highlight the knowledge gap between understanding the thermoelectric properties and the formation of TMDC heterojunctions, as this ultimately concerns the application of TMDC as an effective active layer in thermoelectric generators. In here, we aim to communicate the thermoelectric properties of $MoS_2/MoSe_2$ atomic heterojunction, taking as the starting point the fabrication of a $MoS_2/MoSe_2$ multilayer system through RF-sputtering. Thin-film heterojunction exhibited *n*-type semiconductor behavior with thermally activated charge carriers as well as a compelling Seebeck coefficient; moreover, a series of computational calculations for $MoS_2/MoSe_2$ heterojunction models, in order to provide theoretical explanation of experimental results, emphasize thermoelectric and electronic performance of two-dimensional material heterojunctions.

Results and discussion

Thin-film fabrication of $MoS_2/MoSe_2$ heterojunction

A cross-sectional view of the $MoS_2/MoSe_2$ deposit indicates a clear and well-defined junction between the two materials (Fig. 1a) with a total thickness of approximately 1.6 μm, whereas the surface of the thin film has a fringe-like structure, which agrees with previous reports.[5,6] Each transition metal dichalcogenide layer has an approximate thickness of 800 nm, as recorded by a profilometer (Fig. S1). In scanning Electron Microscopy (SEM) images, a fringe-like structure was observed, which corresponds to the preferential growth of the $MoSe_2$ and MoS_2 layers along [101]-direction, with vertical alignment and Atomic Force Microscopy (AFM) also confirms rough surface and thickness. To further corroborate this, Raman spectroscopy indicates vibrational modes at ~ 400, ~ 411, and ~ 375 cm^{-1} corresponding to the A_{1g} and E^1_{2g} vibrational modes of MoS_2,[21] and for $MoSe_2$, the characteristic modes appear at 242 and 281 cm^{-1} (Fig. S2). The signals at ~ 335 and ~ 275 cm^{-1} correspond to the blue-shifted E_1 and A_1 modes, respectively, owing to the formation of the MoSSe phase at the junction.[9] From the relation between the A^1_g and E^1_{2g} peaks, we can indicate that the material has preferential grain growth in the vertical direction due to a greater out-of-plane signal induced by the vertically aligned material.[21,22] X-ray diffraction shows the presence of peaks of 2θ at ~ 15° and ~ 28° (Fig. 1c), along with the peaks of the polyamide flexible substrate at ~ 18° and ~ 22° 2θ. The aforementioned peaks are directly associated with (002)-basal plane of both MoS_2 and $MoSe_2$ confirming formation of a 2H-MoX_2 phase (where X = S or Se); however, SEM and broader XRD peaks indicate and confirm large colonies of MoS_2 and $MoSe_2$ grains and surface porosity.[21] Hard X-ray photoelectron spectroscopy (HAXPES) was used to identify the elemental composition for near the surface of the $MoS_2/MoSe_2$ sample (Fig. S3 presents the survey spectrum of the sample). Detection of Mo $3d_{5/2}$ and Mo $3d_{3/2}$ core levels at binding energy (BE) values of 229.3 ± 0.1 and 232.4 ± 0.1 eV, respectively (Fig. 1d), agrees with BE values reported for MoS_2 in literature.[23] Additionally, more than one S 2 s peaks can be detected adjacent to the Mo 3d core levels, indicating several sulfur chemical environments at the surface of the sample. The more obvious of these S-related peak contributions (i.e., those not fully overlapping with the Mo 3d lines) is found at BE values of 226.0 ± 0.2 eV and 234.3 ± 0.2 eV, respectively. These BE values correspond to sulfur compounds with oxidation states of − 2 (e.g., sulfides) and + 6 (e.g., sulfates), respectively; and sulfur oxidation state of − 2 corresponds to MoS_2 composition, whereas the minor signal is related to a sulfur oxidation state of + 6 due to exposure to air conditions. HAXPES detail spectra of the Se $2p_{3/2}$ and Se 3d energy regions are presented (Fig. S3a and b). The fact that Se-related signal can be detected via HAXPES at the surface of the 800-nm-thick MoS_2 layer is likely due to anion diffusion/intermixing across the heterojunction, in line with the above-mentioned Raman results, indicating the formation of the MoSSe phase at the junction. Finally, Transmission Electron Microscopy (TEM) also confirms typical fringes, vertical alignment, and random orientation of MoS_2–$MoSe_2$ layers (Fig. 1f); however in bulk thin film, a well-defined heterojunction has been is achieved by our "*one-step*" scalable fabrication method[6,7,10,27] and Focus Ion Beam-SEM images for *"lift-out"* process in Fig. S4.

Thermoelectric response of $MoS_2/MoSe_2$ heterojunction

The generated voltage as a function of temperature indicates the existence of a Seebeck effect, considering the relation given by the following equation:

$$S = -\frac{\Delta V}{\Delta T}, \tag{1}$$

where ΔV is the open-circuit voltage measured and ΔT is the applied temperature gradient. Then, the slope of the 2nd order polynomial fit of the voltage vs. temperature gave us the estimation of a Seebeck coefficient of ~ − 1.1 mV K^{-1} for our heterojunction at a ΔT = 40 K (Fig. 2a). Here, negative slope confirms semiconducting *n*-type heterostructure, with maximum generated voltage at 290 K, in agreement with similar reports[15,23,24] and consistent with computational study as discussed in next sections.

The heterojunction's activation energy (E_A) was estimated using the relationship between the measured conductivity (σ) results, and Arrhenius equation is expressed by the following equation:

$$\sigma = Ce^{\frac{-E_A}{k_b T}}, \tag{2}$$

where C is a constant, and k_b and T are the Boltzmann constant and the absolute temperature, respectively, as in agreement

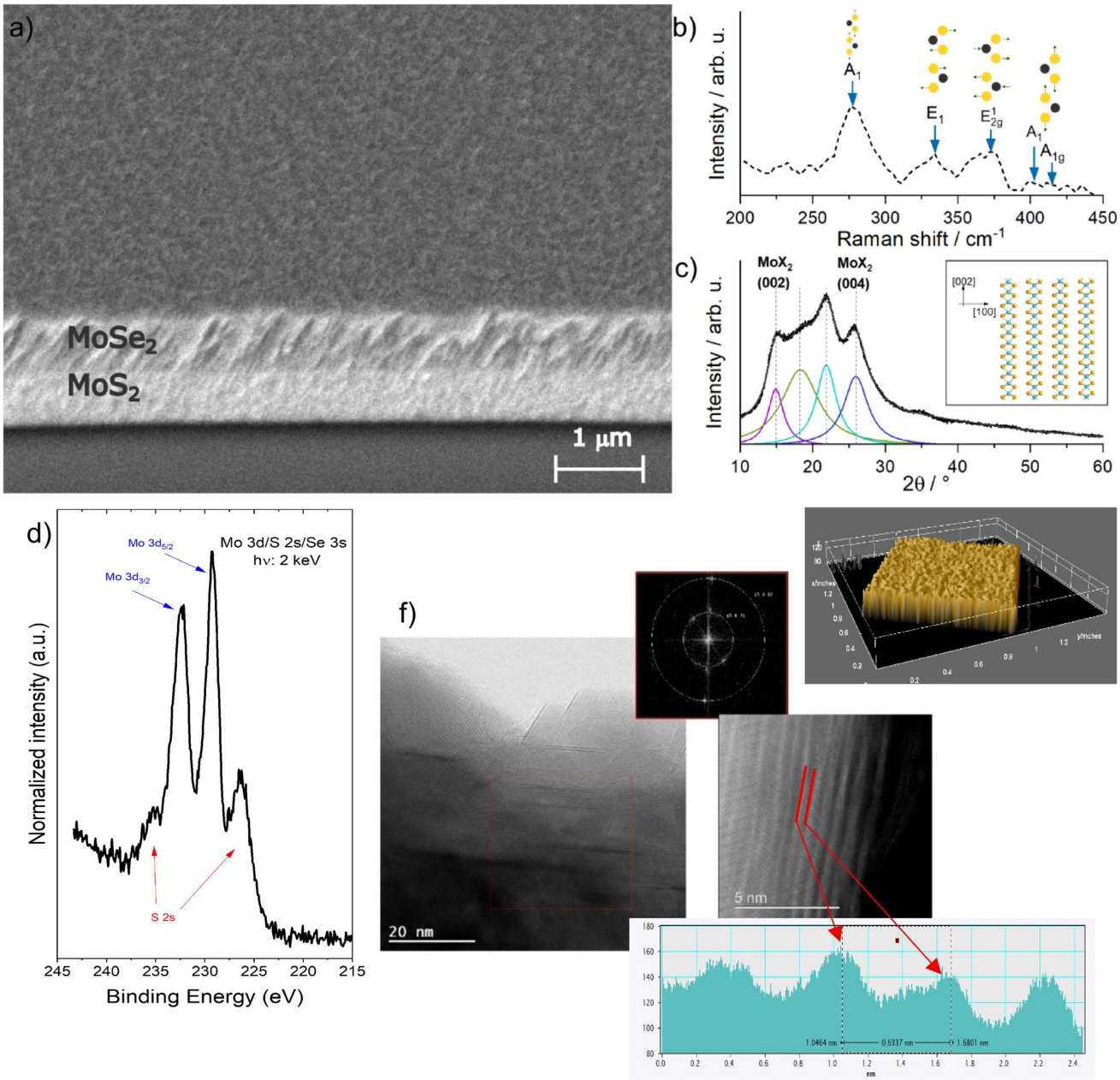

Figure 1. (a) Cross-sectional SEM image of the $MoS_2/MoSe_2$ heterojunction as a thin film with an approximate height of the film of 800 nm, (b) Raman spectroscopy showing the active modes detected for the deposited thin film, and (c) X-ray diffraction pattern of the fabricated heterojunction showing a preferential growth of the film in the direction of the (002) plane for both MoS_2 and $MoSe_2$ labeled as MoX_2 in the figure (inset showing the layered structure of MoS_2 with the exposed (002) and (100) planes). (e) HAXPES details spectrum in the Mo 3d/S 2 s/Se 3 s energy range as measured using 2 keV excitation for the $MoS_2/MoSe_2$ heterojunction. (f) High-resolution transmission electron microscopy confirming the existence of layered fringes with $d_{spacing} \sim 0.63$ nm characteristic of MoS_2 and $MoSe_2$ molecular structures. Atomic Force Microscopy indicates the rough surface which corresponds to needle-like colonies of vertical aligned grains.

with.[16,23,24] The heterojunction exhibits an activation energy of 32.5 meV, as plotted in Fig. 2b, indicating different transport mechanisms within heterojunction as a function of temperature, as reported for MoS_2.[17] Furthermore, the order of magnitude of the extracted activation energy is comparable to the thermal energy at room temperature, suggesting an ease of activation of charge carriers.

The expected relationship between σ and kT suggests a complex transport mechanism in our material; however, the overall trend indicates that thermally activated charge carriers are predominantly dominated by diffusive transport, meaning that charge carriers experience frequent scattering.[16,25,26] This observed complexity is mainly due to the existence of a layered structure and the formation of a heterojunction. Thus, at

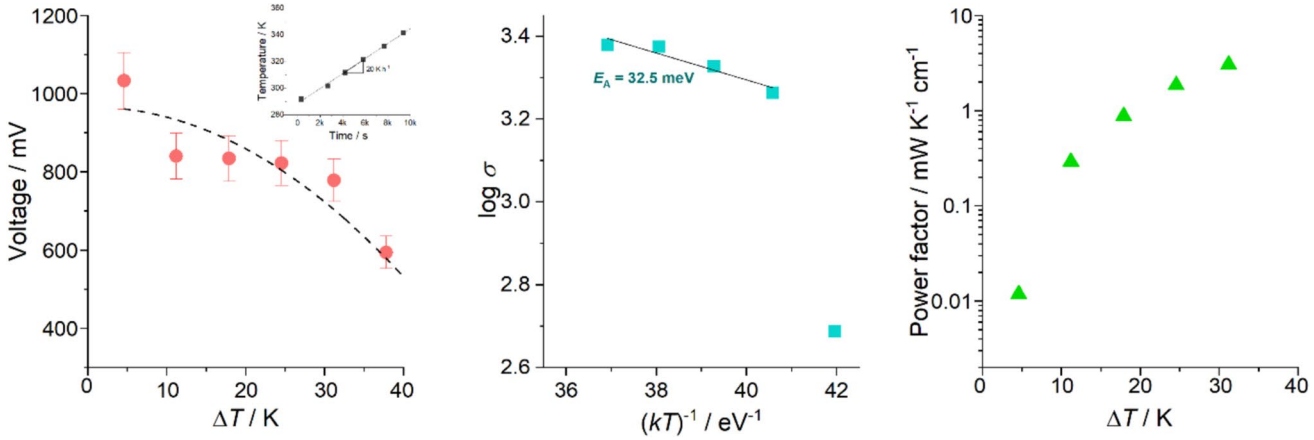

Figure 2. (a) Voltage vs. temperature plot with polynomial fit is an estimation of the Seebeck coefficient for $MoS_2/MoSe_2$ heterostructure $\left(\frac{\Delta V}{\Delta T}\right)$, inset is programmed heating ramp used for thermoelectric measurements with thin-film analyzer (TFA). (b) Conductivity vs. inverse temperature, the slope of the linear region indicates the activation energy (E_A), and the solid line is the polynomial fit, (c) Computed power factor using $PF = S^2\sigma$ equation.

temperatures below 300 K or high $(kT)^{-1}$, the film's transport mechanism may be due to in-gap impurities, whereas at temperatures above 300 K or low $(kT)^{-1}$, charge carrier transport across the band gap due to the temperature gradient may become dominant. Furthermore, the computed power factor ($PF = S^2\sigma$) displays a sharp decrease as the temperature increases, in line with the fact that as the temperature increases, the electron–phonon scattering process becomes dominant,[15] and the Seebeck coefficient decreases, overcoming the increase in electrical conductivity observed previously (Fig. 2c) and helping to confirm a diffusive transport.

The dimensionless figure-of-merit (ZT) value of a material is a fundamental parameter used to compare different thermoelectric materials at a given temperature. The ZT value can be computed using Eq. 3 and relates the electronic transport and thermal transport as follows:

$$ZT = \frac{\sigma S^2}{\kappa} T, \tag{3}$$

where σ is the electrical conductivity, S is the computed Seebeck coefficient, κ is the thermal conductivity, and T is the absolute temperature. The ZT values for our fabricated heterojunction were computed indirectly, considering that $\kappa = \rho D C_p$, where ρ is the density of our thin film, D is the thermal diffusivity, and C_p is the temperature-dependent heat capacity. Details on these calculations are provided in the Supplemental Material (Table S1), and the resulting values of thermal conductivity are in good agreement with available data in the literature.[15,28,29] Then, this results in an approximate ZT value of ~ 1.0 at ~ 330 K, which is a high value of thermoelectric performance compared to state-of-the-art ZT values of ~ 1.3 (@400 K) for $Cu_xPbSe_{0.99}Te_{0.01}$ alloys] ~ 1.8 for n-type PbTe (@773 K),[24] and ~ 0.9 for InP.[30,31] This predicted ZT value indicates that our material has the potential to be implemented in technologies like low-grade waste heat recovery and powering small electronic devices,[30,32–34] although almost an order of magnitude lower than the value we compute when solving the Boltzmann transport equation (BTE) with BoltzTraP2.[52] We then sought to describe the observed dominant transport mechanism and divergence between ZT values using computational modeling through density functional theory in conjunction with the BTE, as discussed in the next section.

Electronic and thermoelectric properties of bulk MoS_2 and $MoSe_2$ by computational methods

We began by validating our DFT calculations using MoS_2 and $MoSe_2$ unit cells. The lattice parameters of the unit cell models of MoS_2 and $MoSe_2$, after the structural optimization, resulted in excellent agreement with the experimentally reported values, and the partial density of states (PDOS) of the MoS_2 and $MoSe_2$ indicates that conduction and valence bands are populated by the p and d orbitals from the chalcogen and the molybdenum, in agreement with previous reports (Table 1) and with.[9,16,25,35] From the computed band structures, we extracted the effective mass of the electrons (m_e^*) in the conduction band (K→Γ) for bulk MoS_2 and $MoSe_2$. Considering parabolic bands, we have that

$$m_e^* = \hbar^2 \left(\frac{d^2E}{dk^2}\right)^{-1}, \tag{4}$$

where $\hbar$ is the reduced Planck's constant. The resulting values of the effective mass for bulk MoS_2 and $MoSe_2$, in units of electron mass at rest (m_0), in agreement with previous reports,[27,36] are displayed in Table 1. In terms of the computed thermoelectric properties, both MoS_2 and $MoSe_2$ resulted in a computed value of the figure-of-merit ZT, which decreased as the temperature increased, dropping to a maximum of 3.4 and 3.1 at 200 K to 3.0 and 2.6 at 500 K for MoS_2 and $MoSe_2$, respectively (Figs. S5 and S6). Our Seebeck coefficient values are consistent with those

Table 1. Resulting structural, electronic, and thermoelectric properties, and comparison with available data of the MoS_2 and $MoSe_2$ unit cells, and MoS_2/$MoSe_2$ heterojunctions.

Structure	a nm^{-1}	c nm^{-1}	ρ g^{-1} cm^{-3}	E_g eV^{-1}	E_{form} eV^{-1}	m_e*	ZT	S	Method	References
MoS_2—unit cell	0.31826	1.354865	4.47356	1.36	N/A	0.534	2.9	1.58 mV K^{-1} (300 K)	DFT	This work
$MoSe_2$—unit cell	0.326511	1.313258	6.95395	1.00	N/A	0.667	2.5	1.54 mV K^{-1} (300 K)	DFT	This work
MoS_2/$MoSe_2$ Random heterojunction	0.322737	1.36160	5.27935	1.15	−7.036	0.708	1.45	1.58 mV K^{-1} (300 K)	DFT	This work
MoS_2/$MoSe_2$ heterojunction	–	–	5.7800	–	–	–	~1.0	1.1 mV K^{-1} (300 K)	Exp	This work
MoS_2/$MoSe_2$ Van Der Waals heterojunction	0.319	8.500	–	0.7	–	–	–	1.3 mV K^{-1} (300 K)	DFT	Lopez-Galan et al.[9]
MoS_2— single layer	–	–	–	–	–	–	–	30 mV K^{-1} (280 K)	Expt	Wu et al.[25]
MoS_2—amorphous	–	–	–	–	–	–	0.03	345–160 μV K^{-1} (300–400 K)	DFT	Lan et al.[15]
MoS_2—single layer	–	–	–	–	–	–	–	~100 μV K^{-1} (–)	Expt	Buscema et al.[8]
MoS_2—single layer	3.18	–	–	1.6	–	–	0.21	1000 μV K^{-1} (300 K)	DFT	Sharma et al.[18]
MoS_2/$MoSe_2$ lateral heterojunction	–	–	–	–	–	–	~1.0	3 mV K^{-1} (300 K)	DFT + non-equilibrium Green's function	Jia et al.[10]

reported by Sharma et al. using DFT methods,[18] although computed for single-layer MoS_2 (Table 1). The values differ by half for those presented by Jia et al. for single-layer MoS_2 at 300 K, with Seebeck coefficients for single-layer MoS_2 of ~ 3 mV K^{-1} at 300 K, but with periodic conditions only in the x direction of the supercell, which may influence the computed transmission function L^{α} inside the Boltzmann transport equation.[10] Nevertheless, our values are in agreement with reports from Wu et al. which indicates for Seebeck coefficient of bulk MoS_2 should be one order of magnitude less in comparison with single-layer MoS_2 at 300 K.[16]

Electronic and thermoelectric properties of MoS_2/$MoSe_2$ heterojunctions by computational methods

Next, we computed the electronic structures of the heterojunction configuration. The computed band structure of the random heterojunction exhibited intermediate values between those of MoS_2 and $MoSe_2$ (Figs. S5 and S6). The random heterojunction presents a band gap of 1.15 eV (Table 1). This band gap decrease represents a reduction of ~ 15% of the band gap compared to pure MoS_2. From the PDOS plots, a change in the contribution of each orbital to the conduction and valence bands can be observed. A strong metallic nature (high contribution of Mo *d* orbitals) arises for both the conduction and valence bands, indicating a substantial decrease in the contribution of the chalcogen. Although the relationship between metallic and chalcogen ions is conserved as a stoichiometric TMDC, the distribution of chalcogen ions affects the electronic distribution of the orbitals. The former observation of a change in the nature of the valence and conduction bands can be understood as the decoupling of the *p* and *d* orbitals around the Fermi level. This decoupling is supplemented by an overlap between chalcogen *p* orbitals from both S and Se atoms, even though no direct bonding occurs between chalcogen species after the structural optimization of the heterojunctions.

The resulting thermoelectric properties of the heterojunctions align with the trend observed in the bulk models of MoS_2 and $MoSe_2$; the Seebeck coefficient (*S*) value decreases as the temperature increases, as expected for *n*-type semiconductors as well as for the MoS_2 and $MoSe_2$ bulk models (Fig. 3). The maximum value of *S* (1.58 mV K^{-1}) occurs at 200 K for the heterojunction, which is slightly larger than that of bulk MoS_2 and $MoSe_2$ and is in the same order of magnitude as our experimental values.

We can relate this behavior to the change in the effective mass of electrons at the conduction band owing to heterojunction formation computed using Eq. 4. As displayed in Table 1, the effective mass of electrons increased to 0.7 compared to bulk MoS_2 and $MoSe_2$. Because the Seebeck coefficient relates to the effective mass as

$$S \propto m_e^* \cdot n^{-\frac{2}{3}}, \tag{5}$$

where *n* is the charge carrier concentration. Therefore, the heavier the electrons become, the Seebeck coefficient increases. As the temperature increases, the Seebeck coefficient decreases, because, in the Boltzmann transport equation, a broader energy distribution of carriers is generated at higher temperatures.

It is predicted that MoS_2/$MoSe_2$ heterostructure facilitates the spatial separation of electrons and holes across the interface, as reported previously.[9] Moreover, at lower temperatures and carrier concentrations, band alignment can enhance the thermoelectric performance by selectively allowing high-energy carriers to contribute to transport. However, as the temperature increases, it is anticipated that *S* decreases because thermal excitation enables a broader range of carriers to participate, diminishing the selectivity of high-energy carriers. This contrasts with $MoSe_2$-based heterojunctions with bismuth telluride, which

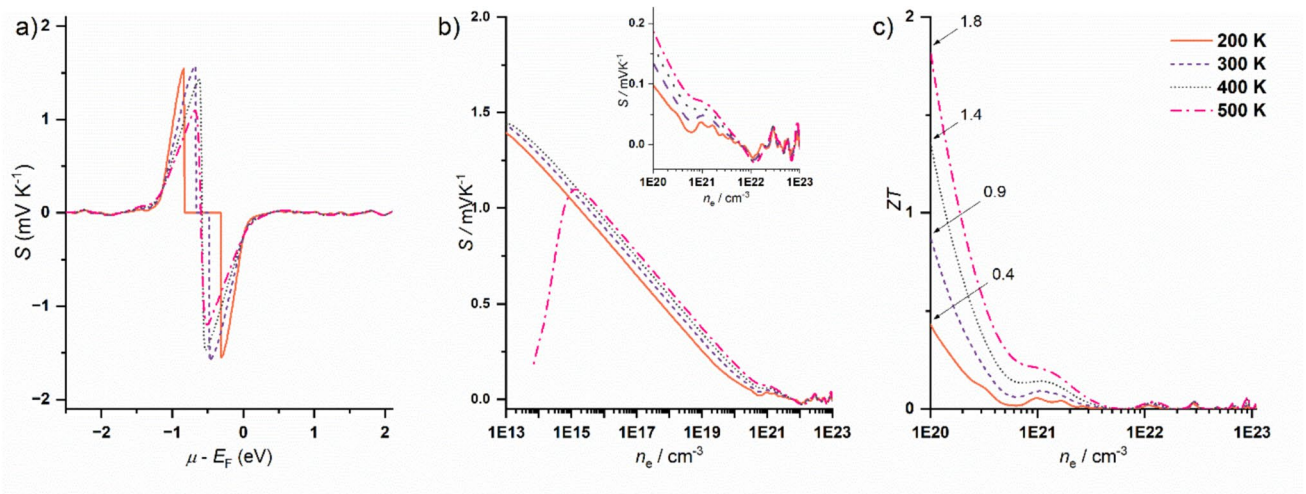

Figure 3. Computed Seebeck coefficient (*S*) as a function of chemical potential (a) and concentration (b) at different temperatures for the heterojunction models. The inset shows a close-up at charge carrier concentrations above 1×10^{19} cm^{-3}. (c) Computed *ZT* value at different temperatures for the modeled heterojunction.

have been demonstrated to maintain or even enhance thermoelectric performance at elevated temperatures due to persistent energy filtering effects at semi-coherent interfaces.[28–31,37,38] The observed temperature dependence of the Seebeck coefficient for our heterojunctions suggests that transport is primarily diffusive, following experimental observations, meaning that the majority of charge carriers (*electrons in this case*) experience frequent scattering events with phonons, impurities, and interface roughness. The mean free path of carriers is shorter than the length scale of the heterojunction, and the flow of electrons follows diffusive mechanisms governed by concentration or thermal gradients. Consequently, the thermally generated voltage is attributed to differences in the carrier energy distribution, rather than to ballistic transport or tunneling across the interface.[28,31,32,39,40] As scattering intensifies with temperature, especially via phonon interactions, the carrier mobility should decrease, further reducing the Seebeck coefficient and confirming a diffusive transport regime.

Nevertheless, the calculation of the Seebeck coefficient as a function of charge carrier concentration suggests that our heterojunction configuration can maintain thermoelectric performance at temperatures above 300 K due to persistent energy filtering effects attributed to interface formation.[31,39] The Seebeck coefficient as a function of concentration shows a significant variation between MoS_2 and $MoSe_2$ (Fig. S7), especially at high temperatures and high concentrations. Meanwhile, the random heterojunction reaches values of $S = 0.19\ mV\ K^{-1}$ at charge carrier concentration of $1 \times 10^{20}\ cm^{-3}$ at 500 K. In contrast, the ZT values of the heterojunction decreased exponentially as the carrier concentration increased, but they increased as the temperature increased for all the heterojunctions (Fig. 3). The maximum value of ZT for the modeled heterojunction is 1.75 at 500 K. The resulting values of ZT indicate that at low carrier concentrations, the heterojunction selectively enhances the thermoelectric power by filtering high-energy carriers, as suggested in the previous paragraphs.[40,41] This is similar to Zhang et al. report, where the authors attribute ZT values for a metastable cubic "ϖ" phase of SnSe of 1.0 at 300 K and up to 3.0 at 800 K to intra-band tunneling transport, which decreases thermal conductivity.[44] This ZT value for our heterojunction model differs from the predicted experimental values of ~ 1.0 presented in the first section; however, this can be attributed to a lower charge carrier concentration in our fabricated heterojunction, as expected in lab-growth TMDC, compared to the computational models.[9,31,42,43,45] Nonetheless, it is assumed that, as the charge carrier concentration and temperature increase, diffusive transport dominates, taking the thermoelectric performance to zero, which is what is occurring in both observations. This is an indication that the interface between MoS_2 and $MoSe_2$ facilitates thermal transport.

As the electrical conductivity is expressed as $\sigma = nq\mu$, where n is the carrier concentration, q is the charge, and μ is the carrier mobility, which is equal to

$$\mu = \frac{q\tau}{m_e^*}, \tag{6}$$

where τ is relaxation or scattering time. From here, we observe that the carrier concentration plays a more significant role in the electrical conductivity of the heterojunctions compared to other effects due to the interface formation, like the increase in the effective mass; however, at high temperatures, the thermal conductivity dominates for our heterojunctions, diminishing the thermoelectric power and taking the material into a highly diffusive transport regime. This implies that the optimization of the conductivity properties of $MoS_2/MoSe_2$ heterojunctions can be addressed by proper doping of the material as used in Mg_3Sb_2 or Cu_4TiSe_4.[45,46]

The random phase of $MoS_2/MoSe_2$ makes this material extremely attractive compared to single-layer TMDC, with the advantage of single one-step fabrication methods, as reported in previous reports.[7] The potential use of $MoS_2/MoSe_2$ heterojunctions in thermoelectric applications is demonstrated by these results. Nevertheless, this shows us that a trade-off among electrical conductivity, thermal conductivity, and Seebeck coefficient is occurring, and charge carrier concentration can be a novel strategy to tune the thermoelectric performance of TMDC thin films.[47]

Conclusions

This study demonstrates the promising thermoelectric capabilities of heterojunctions fabricated via a scalable radiofrequency (RF) sputtering technique. The as-fabricated thin-film heterostructure exhibited *n-type* semiconductor behavior with an outstanding experimental Seebeck coefficient of $-1.1\ mV\ K^{-1}$ at $\Delta T = 40$ K, alongside a low charge carrier activation energy. This performance projects an approximate experimental dimensionless figure-of-merit (ZT) value of ~ 1.0 in the range of 290–330 K. Computational modeling corroborates these findings, predicting a maximum of ZT at higher temperatures for the random heterojunction model, a value higher than the experimental result, which is attributed to lower charge carrier concentrations in the lab-grown material. The measurements confirm a diffusive transport regime in $MoS_2/MoSe_2$ heterojunction, characterized by strong "*electron–phonon*" scattering in the lattice that intensifies when temperature is increased, leading to a decrease in the Seebeck coefficient. This suggests a transition from energy-filtered effects (*at low carrier concentrations*) to bulk-like diffusive transport, which ultimately dominates and facilitates thermal transport at high temperatures/concentrations. These combined insights establish heterojunctions as a compelling platform, demonstrating that charge carrier concentration and interface engineering offer an attractive strategy to tune the conductivity properties and optimize thermoelectric performance for next-generation, low-grade waste heat recovery and energy-harvesting applications.

Methods

Thin-film fabrication of $MoS_2/MoSe_2$ heterojunction

MoS_2 and $MoSe_2$ heterojunctions ($MoS_2/MoSe_2$) were deposited using radio frequency (RF) sputtering in Kurt J. Lesker PVD 75 machine with commercial targets at 99.9% purity, following previous works[5–7]; MoS_2 and $MoSe_2$ have an intrinsically *n*-type semiconductor character, attributed primarily to sulfur vacancies and dangling bonds at the edge of grain boundaries.[47] Thus, the $MoS_2/MoSe_2$ multilayer thin film resembles an *nn*-heterojunction. The $MoS_2/MoSe_2$ multilayer thin film was deposited directly on a polyamide flexible substrate mounted on a Si wafer with a 4 in (1 016 mm) diameter and a thickness of 500 µm (Fig. 4). During the fabrication, we set a vacuum pressure of 1×10^{-4} Pa with an RF power of 200 W at 13.56 MHz. We proceeded with the sequential deposition of MoS_2 after $MoSe_2$, without breaking the vacuum, to achieve a high-quality, contaminant-free $MoS_2/MoSe_2$ multilayer thin film. The target thickness of the $MoS_2/MoSe_2$ was 800 nm, with a dwell rate of ~ 0.3 nm s^{-1}. Once the deposition was completed, the polyamide flexible substrate was unmounted on the Si wafer and kept under vacuum conditions.

Characterization of the $MoS_2/MoSe_2$ heterojunction as a thin film

The obtained p-Si/MoS_2/$MoSe_2$ multilayer structure was characterized using scanning electron microscopy (SEM) to reveal the morphological aspects of the thin film. A Nova 600 Nanolab from FEI Company was used, setting a tilt angle of 45 deg with a working voltage of 5 kV to avoid damage to the material, and a working distance of 4.4 mm with magnifications of 15,000 × and 30,000 ×. Meanwhile, Raman spectroscopy was performed using a laser with a wavelength of 532 nm, with measurements of 10 points with an integration time of 0.64 s. Raman spectroscopy was taken at room temperature with no further sample preparation. X-ray diffraction (XRD) was performed using an X-Pert Pro machine from Panalytical with a $Cu_{k\alpha}$ = 0.15405980 nm, a voltage of 35 kV, and a measured current of 25 mA. The sample was measured from 10 to 80 deg of 2θ using a step time of 30 s and step size of 0.016 deg. Similarly, the XRD measurements were performed at room temperature without further sample preparation. High-resolution transmission electron microscopy was performed using a field emission Cs-corrected STEM unit model 2200-JEOL®, equipped with high-angle annular, dark-field (HAADF) detector, X-Twin lenses, and CCD camera operated at 200 kV, and Atomic Force Microscopy was obtained using a Nanoscope IIIa Digital Instruments® using

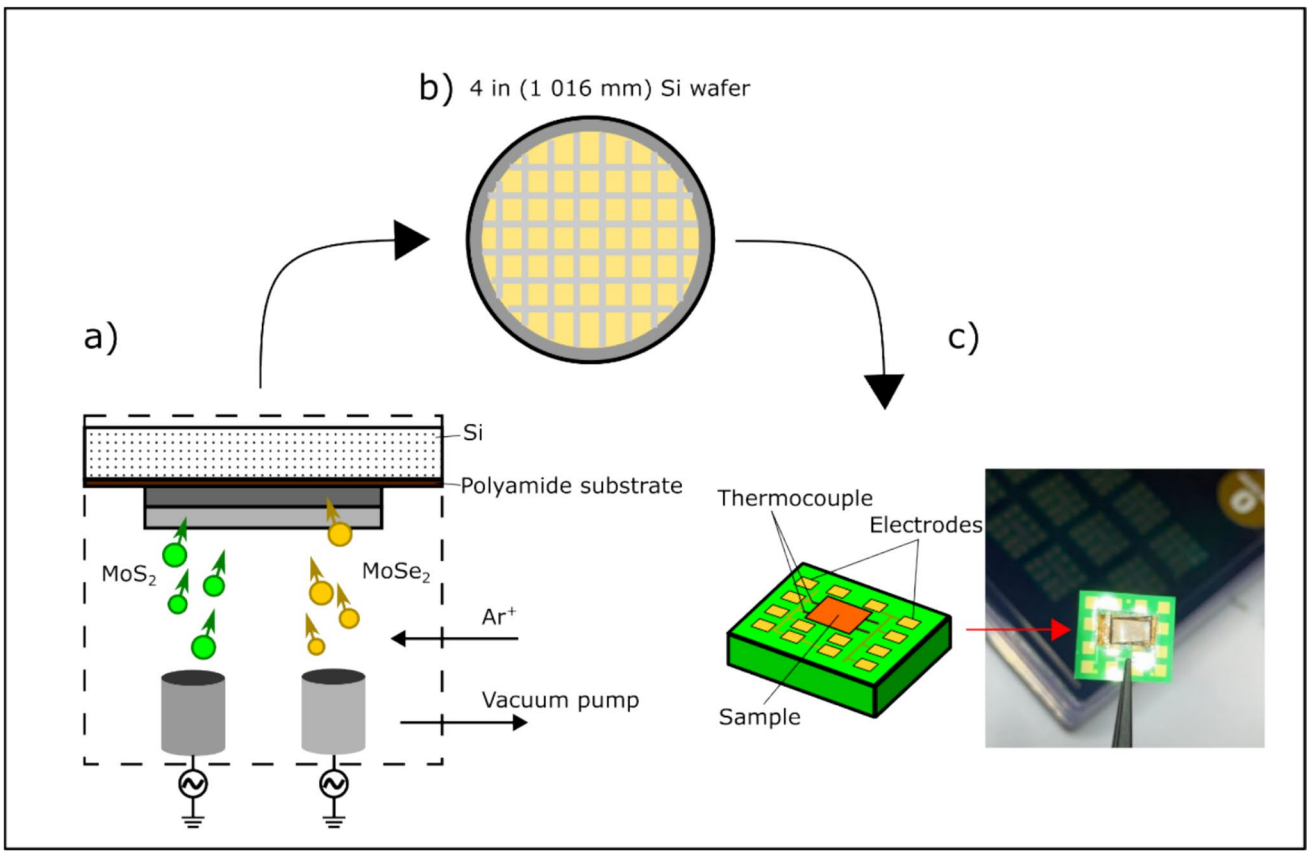

Figure 4. (a) Simplified schematic showing the process of RF-sputtering of the $MoS_2/MoSe_2$ heterojunctions as a thin film. (b) Schematic of the Si wafer used as a support substrate for the RF-sputtering process, (c) photograph of the chip-based platform from Linseis with the sample mounted and schematic of the chip-based platform from Linseis showing the main components of the chip.

a carbon coated probe. Hard X-ray photoelectron spectroscopy (HAXPES) measurements were carried out at the HiKE endstation located at the BESSY II KMC-1 beamline at Helmholtz-Zentrum Berlin (HZB).[53,54] The HiKE endstation is equipped with a Scienta R4000 electron analyzer, and two different excitation energies were used, exploiting different diffraction orders of the Si (111) crystal pair of the KMC-1 double crystal monochromator (i.e., 2 keV in 1st order and 6 keV in 3rd order). The binding energy (BE) scale of the HAXPES measurements was calibrated by measuring the Au 4f energy region of a clean Au foil in electrical contact with the (grounded) sample and setting the BE of the Au $4f_{7/2}$ line to 84.0 eV.

Thermoelectric measurements

We operated a Thin Film Analyzer (TFA) from Linseis Inc. to measure the electrical conductivity and Seebeck coefficient of the $MoS_2/MoSe_2$ heterojunction thin film within the temperature range of 290–330 K, setting a heating rate of 20 K h^{-1} and using the chip-based platform from Linseis, Inc. The thin-film sample was mounted on the chip-based platform provided by the manufacturer for thermoelectric measurements, using silver paste as an adhesive. These chips came with built-in thermocouples and heating elements to run the experiments, which were in direct contact with the fabricated $MoS_2/MoSe_2$ heterojunction, avoiding undesired influence from the substrate (Fig. 4).

Computational calculations

All DFT calculations were performed using the Quantum ESPRESSO package 7.3,[48] the generalized gradient approximation (GGA), and the Perdew–Burke–Ernzerhof (PBE) exchange–correlation functional. The electronic description of the materials was performed through plane-augmented wave (PAW) pseudopotentials provided as included in the SSSP package (1.2.1 version).[49] Structural visualization and handling of the heterojunction model were supported by VESTA[50] and XCrysden codes.[51] For the structural optimization calculations, we employed a plane-wave cutoff energy of 885 eV and a self-consistent field (SCF) energy value of 1.6×10^{-8} eV $atom^{-1}$. The criterion of ionic minimization achieved convergence when all forces were smaller than 8.3×10^{-3} eV nm^{-1} and the total energy changes less than 6.5×10^{-3} eV $atom^{-1}$ in two consecutive self-consistent field steps. A k-point set of dimensions $4 \times 8 \times 4$ was used to sample the Brillouin zone for the heterojunction model. For the structural optimization of the $MoS_2/MoSe_2$ phases, all the atoms and lattice could move freely without constraints. For the density of states (DOS), partial density of states (PDOS), and band structure (BS) calculations, a k-point set of $8 \times 16 \times 8$ with a cutoff energy of 1.09×10^3 eV and an SCF energy value of 1.6×10^{-8} was used to improve the accuracy and detail of the calculations. The electronic structure calculations were performed using optimized structures of the heterojunction model (Fig. 5).

All models started with an optimized MoS_2 unit cell with space group $P6_3/mmc$ and lattice constants $a = b = 0.3168$ nm, $c = 1.2491$ nm, $\alpha = \beta = 90°$, and $\gamma = 120°$, with a Mo–S bond distance ($d_{Mo\text{-}S}$) of 0.2406 nm. The ionic states of S and Se inside the lattice are S^{2-} and Se^{2-}, respectively, both in a three-coordinate geometry linked to three equivalent Mo^{4+} ions in a trigonal prismatic coordination. Then, we created a $4 \times 2 \times 1$ P1 supercell from this model, containing 16 molybdenum atoms and 32 chalcogen atoms, considering three different heterojunction types in a 1:1 relationship between sulfur and selenium. The lattice parameters of this supercell were $a = 1.2672$ nm, $b = 2.498$ nm, $c = 1.2491$, $\alpha = 90°$, $\beta = 90°$, and $\gamma = 120°$. For the random $MoS_{2-x}Se_x$ phase, the selenium atoms substituted for sulfur atoms were distributed randomly throughout the supercell model. For the stability analysis of the resulted atomic arrangement, we considered the formation energy per atom (E_{form} eV^{-1} $atom^{-1}$) of the $MoS_2/MoSe_2$ interface, representing a simultaneous deposition process where all the atomic species converged to the formation of the targeted $MoS_{2-x}Se_x$ phase. This value was computed using the following equation:

$$E_{form} = \frac{1}{N}\left(E_{MoS_{2-x}Se_x} - \sum_{i=1}^{N} \mu_i\right), \qquad (7)$$

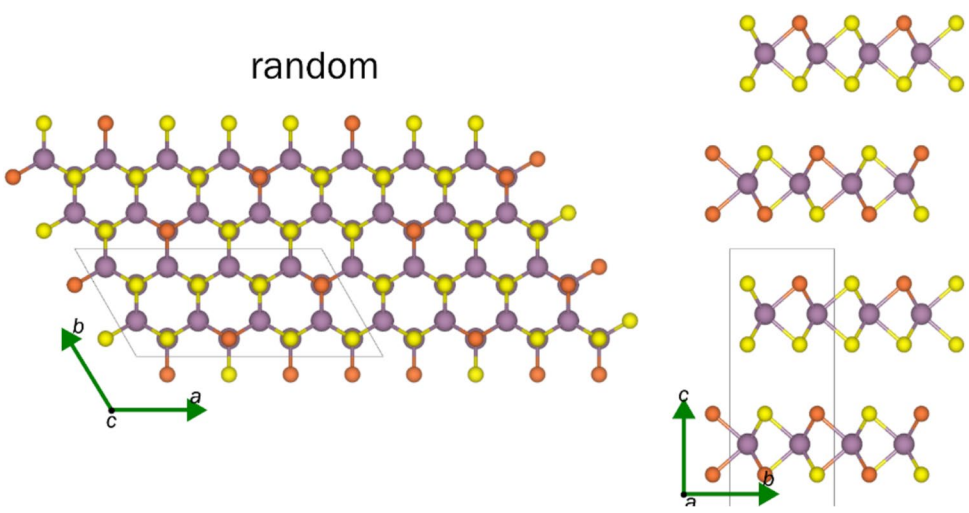

Figure 5. Top-view and side-view of the heterojunction model. The solid black lines represent the boundaries of the supercell used for the calculations.

where $E_{MoS_{2-x}Se_x}$ is the resulting enthalpy of the heterojunction from the structural optimization calculations, N is the total number of atoms, and μ_i is the chemical potential of the i th atom in the phase. For simplicity, the indicated chemical potential was considered as the bulk energy for the conforming atom extracted from the corresponding pseudopotential file. This approach considers that the distribution of selenium and sulfur atoms has an equal probability and that no other type of defect is left in the supercell afterward. The thermoelectric properties were calculated using the BoltzTraP2 code in its 24.9.4 version, which calculates Onsager coefficients by solving the linearized Boltzmann Transport Equation (BTE). Single-point energy calculations from Quantum ESPRESSO were used as input for the BoltzTraP2 code to perform the transport property calculations of the $MoS_2/MoSe_2$ heterojunction. The calculations were carried out in the temperature range of 200–500 K in a − 0.2–0.2 Ha energy interval using a k-point set of 48 × 96 × 48 for improved accuracy for all heterojunction models.

Acknowledgments

Oscar A. López-Galán (OALG) thanks the support from Secretaría de Ciencia, Humanidades, Tecnología e Innovación (Secihti) from Mexico for the postdoctoral fellowship. All authors thankfully acknowledge the high-performing computing resources and support provided by the Baden-Württemberg University Cluster 2.0 (bwUniCluster 2.0) and Baden-Württemberg University Cluster 3.0 (bwUniCluster 3.0). The Energy Materials In-situ Laboratory Berlin (EMIL) operated by the Helmholtz-Zentrum für Materialien und Energie GmbH (HZB) is acknowledged for granting access to its chemistry/sample characterization laboratory. We thank HZB for the allocation of beamtime for HAXPES measurements. OALG recognizes the support from Marco Ramírez from the Department of Chemistry at the University of Texas at El Paso (UTEP) for profile measurements and also special thank Florian Kronast for performing the AFM measurements at EMIL of HZB. This work was performed, in part, at the Center for Integrated Nanotechnologies, an Office of Science User Facility operated for the U.S. Department of Energy (DOE) Office of Science. Sandia National Laboratories is a multi-mission laboratory managed and operated by National Technology & Engineering Solutions of Sandia, LLC, a wholly owned subsidiary of Honeywell International, Inc., for the U.S. DOE's National Nuclear Security Administration under contract DE-NA-0003525. The views expressed in the article do not necessarily represent the views of the U.S. DOE or the United States Government. Manuel Ramos and OALG thank the program Sistema Nacional de Investigadores e Investigadoras from SECIHTI-México, and Dirección General de Investigación y Transferencia Tecnológica (DGITT) from Universidad Autónoma de Ciudad Juárez (UACJ). All authors acknowledge the support from Subdirección de Vinculación e Intercambio Académico from UACJ for the agreement management between UACJ, CINT, KIT, and HZB.

Author contributions

OALG and MR did conceptualization and original draft writing. MR and AR performed thermoelectric measurements at HZB. OALG and FSS performed the fabrication and characterization of thin films. OALG and JLTD performed DFT calculations and analysis. JMG, Jr, and RCAL provided review and analysis. MR, MH, and MT provided revision and research guidance. AHM, L. C. D-R., and R. T-S. supported with HRTEM, and R. F. and M. R. performed HAXPES at HZB. All authors review the final version of this manuscript.

Funding

Open Access funding enabled and organized by Projekt DEAL. Secretaría de Ciencia, Humanidades, Tecnología e Innovación (Secihti) from Mexico for the postdoctoral fellowship "Estancia Posdoctoral por México" number 790769. Project PIISO-401-24-05 from Universidad Autónoma de Ciudad Juárez. The Center for Integrated Nanotechnologies proposal number 2023BU0045.

Data availability

The data that support the findings of this study are available from the corresponding author upon reasonable request.

Code availability

Not applicable.

Declarations

Conflict of interest

The authors have no conflicts to disclose.

REFERENCES

1. D.-H. Baek, J. Kim, MoS_2 gas sensor functionalized by Pd for the detection of hydrogen. Sens. Actuators, B Chem. **250**, 686–691 (2017)

2. M.J. Park, J.K. Min, S.-G. Yi, J.H. Kim, J. Oh, K.-H. Yoo, Near-infrared photodetectors utilizing MoS_2 -based heterojunctions. J. Appl. Phys. **118**(4), 044504 (2015). https://doi.org/10.1063/1.4927749
3. M. Che et al., High-efficiency self-powered broadband photodetector based on $PtSe_2$ /$MoSe_2$ heterojunction. ACS Photon. **11**(4), 1693–1702 (2024). https://doi.org/10.1021/acsphotonics.3c01922
4. M.-L. Tsai et al., Monolayer MoS_2 heterojunction solar cells. ACS Nano **8**(8), 8317–8322 (2014)
5. M. Ramos et al. Organic-semiconducting hybrid solar cell, US 10,727,428, US Patent and Trademark Office (2020). https://www.osti.gov/biblio/1735085. Accessed 15 July 2025.
6. M. Ramos et al., Mechanical properties of RF-sputtering MoS_2 thin films. Surf. Topogr. Metrol. Prop. **5**(2), 025003 (2017). https://doi.org/10.1088/2051-672X/aa7421
7. O.A. López-Galán et al., One-step sputtering of MoSSe metastable phase as thin film and predicted thermodynamic stability by computational methods. Sci. Rep. **14**(1), 7104 (2024). https://doi.org/10.1038/s41598-024-57243-3
8. M. Buscema, M. Barkelid, V. Zwiller, H.S.J. Van Der Zant, G.A. Steele, A. Castellanos-Gomez, Large and tunable photothermoelectric effect in single-layer MoS_2. Nano Lett. **13**(2), 358–363 (2013). https://doi.org/10.1021/nl303321g
9. O.A. López-Galán, I. Perez, J. Nogan, M. Ramos, Determining the electronic structure and thermoelectric properties of MoS_2 /$MoSe_2$ type-I heterojunction by DFT and the Landauer approach. Adv. Mater. Interfaces (2023). https://doi.org/10.1002/admi.202202339
10. P.-Z. Jia et al., Excellent thermoelectric performance induced by interface effect in MoS_2 /$MoSe_2$ van der Waals heterostructure. J. Phys. Condens. Matter **32**(5), 055302 (2020). https://doi.org/10.1088/1361-648X/ab4cab
11. R.C. O'Brien, R.M. Ambrosi, N.P. Bannister, S.D. Howe, H.V. Atkinson, Safe radioisotope thermoelectric generators and heat sources for space applications. J. Nucl. Mater. **377**(3), 506–521 (2008). https://doi.org/10.1016/j.jnucmat.2008.04.009
12. D. Champier, Thermoelectric generators: a review of applications. Energy Convers. Manag. **140**, 167–181 (2017). https://doi.org/10.1016/j.enconman.2017.02.070
13. H.J. Goldsmid, Improving the thermoelectric figure of merit. Sci. Technol. Adv. Mater. **22**(1), 280–284 (2021). https://doi.org/10.1080/14686996.2021.1903816
14. A.F. Ioffe, L.S. Stil'bans, E.K. Iordanishvili, T.S. Stavitskaya, A. Gelbtuch, G. Vineyard, Semiconductor thermoelements and thermoelectric cooling. Phys. Today **12**(5), 42–42 (1959). https://doi.org/10.1063/1.3060810
15. T. Lan et al. The experimental study on the thermoelectric properties of sputtered amorphous molybdenum disulfide films. Nanoscale Microscale Thermophys. Eng. 1–17 (2025). https://doi.org/10.1080/15567265.2025.2458865.
16. S. Ashraf et al., Thermoelectric properties of n-type molybdenum disulfide (MoS_2) thin film by using a simple measurement method. Materials **12**(21), 3521 (2019). https://doi.org/10.3390/ma12213521
17. C. Muratore et al., Thermal anisotropy in nano-crystalline MoS_2 thin films. Phys. Chem. Chem. Phys. **16**(3), 1008–1014 (2014). https://doi.org/10.1039/C3CP53746C
18. M. Sharma et al., Electron transport and thermoelectric performance of defected monolayer MoS_2. Physica E Low-Dimens. Syst. Nanostruct. **107**, 117–123 (2019). https://doi.org/10.1016/j.physe.2018.11.011
19. A. Patel et al., High thermoelectric performance in two-dimensional Janus monolayer material WS-X (X = Se and Te). ACS Appl. Mater. Interfaces **12**(41), 46212–46219 (2020). https://doi.org/10.1021/acsami.0c13960
20. J. Jaiswal, A. Das, V. Chetry, S. Kumar, R. Chandra, NO_2 sensors based on crystalline $MoSe_2$ porous nanowall thin films with vertically aligned molecular layers prepared by sputtering. Sens. Actuators B Chem. **359**, 131552 (2022). https://doi.org/10.1016/j.snb.2022.131552
21. Y.P. Venkata Subbaiah, K.J. Saji, A. Tiwari, Atomically thin MoS_2: a versatile nongraphene 2D material. Adv. Funct. Mater. **26**(13), 2046–2069 (2016). https://doi.org/10.1002/adfm.201504202
22. Z.-H. Chi et al., Pressure-induced metallization of molybdenum disulfide. Phys. Rev. Lett. **113**(3), 036802 (2014). https://doi.org/10.1103/PhysRevLett.113.036802
23. M. Bär et al., Chemical structures of the Cu(In,Ga)Se_2/Mo and Cu(In,Ga)$(S,Se)_2$/Mo interfaces. Phys. Rev. B **78**, 075404 (2008)
24. H. J. Goldsmid, *Introduction to Thermoelectricity*, in Springer Series in Materials Science, vol. 121 (Berlin, Heidelberg, Springer, 2016) https://doi.org/10.1007/978-3-662-49256-7
25. J. Wu, H. Schmidt, K.K. Amara, X. Xu, G. Eda, B. Özyilmaz, Large thermoelectricity via variable range hopping in chemical vapor deposition grown single-layer MoS_2. Nano Lett. **14**(5), 2730–2734 (2014). https://doi.org/10.1021/nl500666m
26. J.L. Blackburn, S.D. Kang, M.J. Roos, B. Norton-Baker, E.M. Miller, A.J. Ferguson, Intrinsic and extrinsically limited thermoelectric transport within semiconducting single-walled carbon nanotube networks. Adv. Electron. Mater. **5**(11), 1800910 (2019). https://doi.org/10.1002/aelm.201800910
27. M. Lundstrom, Fundamentals of carrier transport. Meas. Sci. Technol. **13**(2), 230–230 (2002). https://doi.org/10.1088/0957-0233/13/2/703
28. S. Ippolito et al., Unveiling charge-transport mechanisms in electronic devices based on defect-engineered MoS_2 covalent networks. Adv. Mater. (2023). https://doi.org/10.1002/adma.202211157
29. C. Zhou et al., Exceptionally high average power factor and thermoelectric figure of merit in n-type PbSe by the dual incorporation of Cu and Te. J. Am. Chem. Soc. **142**(35), 15172–15186 (2020). https://doi.org/10.1021/jacs.0c07712
30. L. Fu et al., Large enhancement of thermoelectric properties in n-type PbTe via dual-site point defects. Energy Environ. Sci. **10**(9), 2030–2040 (2017). https://doi.org/10.1039/C7EE01871A
31. J.V. Gajjar, P. Kumar, D.R. Roy, Monolayer group III phosphides (XP; X = B, Al, Ga, and In): structural stability to thermoelectrics and transport properties. Adv. Mater. Technol. (2025). https://doi.org/10.1002/admt.202402145
32. C. Gong, L. Colombo, R.M. Wallace, K. Cho, The unusual mechanism of partial fermi level pinning at metal–MoS_2 interfaces. Nano Lett. **14**(4), 1714–1720 (2014). https://doi.org/10.1021/nl403465v
33. S.K. Mahatha, K.D. Patel, K.S.R. Menon, Electronic structure investigation of MoS_2 and $MoSe_2$ using angle-resolved photoemission spectroscopy and ab initio band structure studies. J. Phys. Condens. Matter **24**(47), 475504 (2012). https://doi.org/10.1088/0953-8984/24/47/475504
34. J.-H. Hwang et al., Improving electrochemical Pb^{2+} detection using a vertically aligned 2D MoS_2 nanofilm. Anal. Chem. **91**(18), 11770–11777 (2019). https://doi.org/10.1021/acs.analchem.9b02382
35. B. Li et al., Preparation of monolayer MoS_2 quantum dots using temporally shaped femtosecond laser ablation of bulk MoS_2 targets in water. Sci. Rep. **7**(1), 11182 (2017). https://doi.org/10.1038/s41598-017-10632-3
36. Y. You et al., Modification of the intermediate band and thermoelectric properties in Se-doped $CoSbS_{1-x}$ Se_x compounds. RSC Adv. **7**(55), 34466–34472 (2017). https://doi.org/10.1039/C7RA05609E
37. J.J. Bae et al., Thickness-dependent in-plane thermal conductivity of suspended MoS_2 grown by chemical vapor deposition. Nanoscale **9**(7), 2541–2547 (2017). https://doi.org/10.1039/C6NR09484H
38. P. Yuan, R. Wang, T. Wang, X. Wang, Y. Xie, Nonmonotonic thickness-dependence of in-plane thermal conductivity of few-layered MoS_2: 2.4 to 37.8 nm. Phys. Chem. Chem. Phys. **20**(40), 25752–25761 (2018). https://doi.org/10.1039/C8CP02858C

39. M.H. Lee, W. Wu, 2D materials for wearable energy harvesting. Adv. Mater. Technol. **7**(9), 2101623 (2022). https://doi.org/10.1002/admt.202101623
40. S.K. Mahatha, K.D. Patel, K.S.R. Menon, Electronic structure investigation of MoS_2 and $MoSe_2$ using angle-resolved photoemission spectroscopy and ab initio band structure studies. J. Phys. Condens. Matter **24**(47), 475504 (2012). https://doi.org/10.1088/0953-8984/24/47/475504
41. H. Peelaers, C.G. de Van Walle, Effects of strain on band structure and effective masses in MoS_2,. Phys. Rev. B **86**(24), 241401 (2012). https://doi.org/10.1103/PhysRevB.86.241401
42. B. Biel, L. Donetti, E.R. Ortiz, A. Godoy, F. Gámiz, Tunability of effective masses on MoS_2 monolayers,. Microelectron. Eng. **147**, 302–305 (2015). https://doi.org/10.1016/j.mee.2015.04.099
43. A. Sood et al., Quasi-ballistic thermal transport across MoS_2 thin films. Nano Lett. **19**(4), 2434–2442 (2019). https://doi.org/10.1021/acs.nanolett.8b05174
44. M. Zhang, I. Pallikara, J.M. Flitcroft, J.M. Skelton, Amorphous-like thermal conductivity and high thermoelectric figure of merit in 'π' SnS and SnSe. J. Mater. Chem. A **13**(7), 5415–5426 (2025). https://doi.org/10.1039/D4TA05815A
45. M. Owais, X. Luo, M. Rehman, R.T. Mushtaq, M. Alkahtani, Investigating Fe and Cr doping effects on thermoelectric efficiency in Mg_3Sb_2 through first-principles calculations for sustainable energy solutions. Sci. Rep. **15**(1), 9419 (2025). https://doi.org/10.1038/s41598-025-92809-9
46. X.-K. Chen, E.-M. Zhang, D. Wu, K.-Q. Chen, Strain-induced medium-temperature thermoelectric performance of Cu_4TiSe_4: the role of four-phonon scattering. Phys. Rev. Appl. **19**(4), 044052 (2023). https://doi.org/10.1103/PhysRevApplied.19.044052
47. S. McDonnell et al., Defect-dominated doping and contact resistance in MoS_2. ACS Nano **8**(3), 2880–2888 (2014)
48. P. Giannozzi et al., Advanced capabilities for materials modelling with Quantum ESPRESSO,. J. Phys. Condens. Matter **29**(46), 465901 (2017). https://doi.org/10.1088/1361-648X/aa8f79
49. G. Prandini, A. Marrazzo, I.E. Castelli, N. Mounet, N. Marzari, Precision and efficiency in solid-state pseudopotential calculations. Npj Comput. Mater. **4**(1), 72 (2018). https://doi.org/10.1038/s41524-018-0127-2
50. K. Momma, F. Izumi, *VESTA3* for three-dimensional visualization of crystal, volumetric and morphology data. J. Appl. Crystallogr. **44**(6), 1272–1276 (2011). https://doi.org/10.1107/S0021889811038970
51. A. Kokalj, XCrySDen—a new program for displaying crystalline structures and electron densities. J. Mol. Graph. Model. **17**(3–4), 176–179 (1999). https://doi.org/10.1016/S1093-3263(99)00028-5
52. G.K.H. Madsen, J. Carrete, M.J. Verstraete, BoltzTraP2, a program for interpolating band structures and calculating semi-classical transport coefficients. Comput. Phys. Commun. **231**, 140–145 (2018). https://doi.org/10.1016/j.cpc.2018.05.010
53. M. Gorgoi et al., The high kinetic energy photoelectron spectroscopy facility at BESSY progress and first results. Nucl. Instrum. Methods Phys. Res. Sect. A Accel. Spectrom. Detect. Assoc. Equip. **601**, 48 (2009)
54. F. Schäfers et al., KMC-1: a high resolution and high flux soft X-ray beamline at BESSY. Rev. Sci. Instrum. **78**, 123102 (2007)